Electron Acceleration during Macroscale Magnetic Reconnection

H. Arnold, J. F. Drake, and M. Swisdak

IREAP, University of Maryland, College Park MD 20742-3511, USA

F. Guo

Los Alamos National Lab, Los Alamos NM 87545, USA

J. T. Dahlin

NASA Goddard Space Flight Center, Greenbelt MD 20771, USA

B. Chen and G. Fleishman

New Jersey Institute of technology, Newark NJ 07102, USA

L. Glesener

University of Minnesota, Minneapolis MN 55455, USA

E. Kontar

University of Glasgow, Glasgow, UK, G12 8QQ

T. Phan

University of California, Berkeley CA, USA

C. Shen

Harvard University, Cambridge MA, USA

(Dated: January 26, 2021)

Abstract

The first self-consistent simulations of electron acceleration during magnetic reconnection in a macroscale system are presented. Consistent with solar flare observations the spectra of energetic electrons take the form of power-laws that extend more than two decades in energy. The drive mechanism for these nonthermal electrons is Fermi reflection in growing and merging magnetic flux ropes. A strong guide field is found to suppress the production of nonthermal electrons by weakening the Fermi drive mechanism. For a weak guide field the total energy content of nonthermal electrons dominates that of the hot thermal electrons even though their number density remains small. Our results are benchmarked with the hard x-ray, radio and extreme ultra-violet (EUV) observations of the X8.2-class solar flare on September 10, 2017.

Introduction Solar flares are explosive events in the solar corona that convert magnetic energy into particle energy through magnetic reconnection [1–4]. While some released magnetic field energy goes into bulk flows and thermal energy, a significant fraction appears in nonthermal electrons, which form a power-law tail in the distribution function [2, 4, 5]. In some cases the pressure from these electrons can approach the ambient magnetic pressure [6, 27]. Observations by the Reuven Ramaty High Energy Solar Spectroscopic Imager (RHESSI) and the Atmospheric Imaging Assembly on the Solar Dynamic Observatory, suggest that these energetic electrons make up a significant fraction of the total electron density in the above-the-loop-top sources in solar flares [13].

Magnetic reconnection creates bent field lines with a tension that drives an exhaust away from the x-line near the Alfvén speed [14, 15], energizing the surrounding plasma. When particles stream into the exhaust, they gain energy by reflecting off the bent field lines [11]. This process is referred to as Fermi reflection and is believed to be responsible for producing the power-law tails in the electron distribution function [11, 16–18]. The energy gain of an electron due to Fermi reflection is proportional to its energy and therefore dominates the energy gain of the most energetic electrons. Fermi reflection does not depend on any kinetic length scale. Rather the relevant length is the curvature of the reconnecting magnetic field. Electrons can continue to gain energy from Fermi reflection even as flux ropes merge and approach the domain size [19].

This paper presents the first results of simulations of particle acceleration during magnetic reconnection in a 2D macrosystem that includes the self-consistent feedback of energetic

particles on the dynamics. The simulation model, *kglobal* [20, 21], retains Fermi reflection as the dominant drive mechanism for energetic electrons but excludes parallel electric fields in kinetic-scale boundary layers. Consequently, the kinetic scales that constrain PIC modeling of macroscale systems are eliminated. For the first time we simulate magnetic reconnection and particle acceleration in domains with sizes that characterize energy release in solar flares. *kglobal* includes the self-consistent feedback of energetic electrons on the large-scale dynamics of reconnection so that the global energy is conserved. While the ordering of *kglobal* eliminates kinetic-scale parallel electric fields, the model includes large-scale parallel electric fields, important for the initial energy gain of electrons during reconnection [23–25].

The *kglobal* simulations produce power-law spectra of energetic electrons that extend nearly three decades in energy and simultaneously produce super-hot thermal electrons that characterize flare observations [6, 26, 27]. Consistent with observations, the total energy content of the nonthermal electrons can exceed that of the hot thermal electrons even though the number density of the nonthermals is less than the hot thermals. Simulations carried out with a variety of values of the initial ambient out-of-plane guide field reveal that the strength of the guide field strongly impacts the energy content of the nonthermal electrons and their power-law index. A guide field exceeding the reconnecting magnetic field suppresses production of nonthermal electrons by weakening the Fermi drive mechanism. In contrast, the size of the global system has relatively little influence on the production of nonthermal electrons.

Numerical Simulations Setup The 2D simulations presented here are carried out with the *kglobal* model, which consists of a magnetohydrodynamic (MHD) backbone with fluid ions and electrons as well as particle electrons that are distributed as macroparticles on the MHD grid. The two electron species combine so that charge neutrality is preserved at all times [20, 21]. However, since the equations governing energy gain in the electron fluid are incomplete (e.g., Fermi reflection is not included), any change in the energy of the electron fluid will be neglected in the analysis of the electron energy gain. The upstream reconnection magnetic field, B_0, and the ion density, n_0, define the Alfvén speed, $C_{A0} = B_0/\sqrt{4\pi m_i n_0}$. Since no kinetic scales are resolved, lengths are normalized to an arbitrary macroscale L_0. Times are normalized to $\tau_A = L_0/C_{A0}$ and temperatures and particle energies to $m_i C_{A0}^2$. The perpendicular electric field follows an MHD scaling, $C_{A0}B_0/c$. The parallel electric field scales like $m_i C_{A0}^2/L_0 e$ and is small compared with the perpendicular component. However,

3

the energy associated with the parallel potential drop acting over the scale L_0 is of order $m_i C_{A0}^2$, which is comparable to the available magnetic energy per particle.

The simulations are initialized with constant densities and pressures in a force-free current sheet and periodic boundary conditions. Thus, $\boldsymbol{B} = B_0 \tanh(y/w)\hat{\boldsymbol{x}} + \sqrt{B_0^2 \operatorname{sech}^2(y/w) + B_g^2}\,\hat{\boldsymbol{z}}$. The temperatures of all three species are uniform and isotropic with $T_i = T_{e,part} = T_{e,fluid} = 0.0625 m_i C_{A0}^2$, leading to an initial plasma β of 0.25 (based on B_0). While the initial β is higher than typical coronal values, electron heating and acceleration is insensitive to this choice as well as to the chosen fraction of particle electrons (25% of the total electrons). The domain size for all simulations is $L_x \times L_y = 2\pi L_0 \times \pi/2 L_0$. The magnetic field evolution equation includes a hyper-resistivity ν to facilitate reconnection, while minimizing dissipation at large scales [28]. The effective Lundquist number $S_\nu = C_A L_0^3 / \nu$ associated with this hyper-resistivity is varied to change the effective system size (ratio of the macro to the dissipation scale). We also include fourth and second order viscosity terms and some electron particle diffusion to prevent a numerical instability associated with trapping electrons in small perpendicular electric field fluctuations. Reconnection begins from particle noise and proceeds to produce multiple flux ropes whose number depends on S_ν, with larger values of S_ν producing more initial flux ropes. However, our late-time results are relatively insensitive to S_ν and therefore the effective system size. Thus, unless otherwise stated we focus on simulations with 100 particles per cell, time step $dt = 0.0001\tau_0$, $S_\nu = 9.5 \times 10^7$, and $N_x \times N_y = 2048 \times 512$ grid cells. By taking $L_0 = 10^4 km$, our grid cell is 30 km across, much larger than any kinetic scales or PIC simulations. The mass ratio is $m_i/m_e = 25$. The results are not sensitive to this value. The speed of light is $c/C_{A0} \approx 60$. We use guide fields $B_g/B_0 = 0.1$, 0.25, 0.4, 0.5, 0.6, 0.8, and 1.0.

Simulation Results Since magnetic reconnection in our simulations is triggered by particle noise, the dynamics begins with the growth of many small islands, which subsequently undergo mergers and eventually approach the system scale. This behavior is seen in Fig. 1 from a simulation with $B_g/B_0 = 0.25$. The energy per particle of the particle electrons, $<W>$ (energy density divided by number density), is shown in the $x - y$ plane at three times, $t/\tau_A = 2.5$, 5, and 8 in panels (a), (b), and (c). Magnetic field lines are superimposed. The particle electron energy is nearly constant along field lines because of the high electron mobility parallel to the magnetic field.

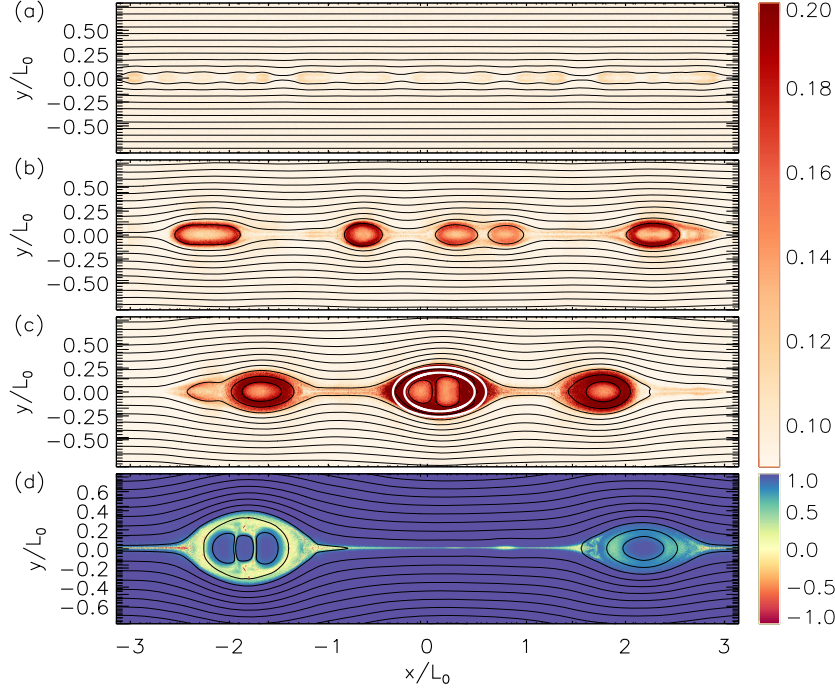The firehose parameter, $1 - 4\pi(P_\parallel - P_\perp)/B^2$, is plotted in Fig. 1(d) at late time from a

FIG. 1. In (a), (b), and (c): $<W>$ for a simulation with $B_g/B_0 = 0.25$ in the $x - y$ plane at $t/\tau_A = 2.5$, 5, and 8 with magnetic field lines overplotted. In (d): the firehose stability parameter at late time from a simulation with $B_g/B_0 = 0.1$.

simulation with $B_g/B_0 = 0.1$. Large regions within the magnetic islands are near marginal stability (with some unstable regions) so that the local magnetic tension, which drives particle energy gain, is largely suppressed within flux ropes in this simulation. Thus, electron feedback on the MHD fluid is essential in regimes where electron energy gain is significant. Models based on test particle dynamics neglect the feedback of particles on the dynamics and can therefore lead to runaway electron energy gain.

The spectrum of nonthermal electrons is calculated from the simulations by summing the total number of particle electrons within a specified energy range over the entire simulation domain. This ensures that we maximize the count rate of the electrons at the highest energies to improve the statistics of the measured distribution. In Fig. 2(a) we plot the differential electron number density $F(W) = dN(W)/dW$ versus the normalized energy, $W/m_i C_{A0}^2$, on a log-log scale at several times for the case $B_g/B_0 = 0.25$ shown in Fig. 1. $F(W)$ takes the form of a power-law (a straight line in the log-log plot) as time progresses. The power-law index δ' reaches a constant value at low energy early and extends to higher energy over time.
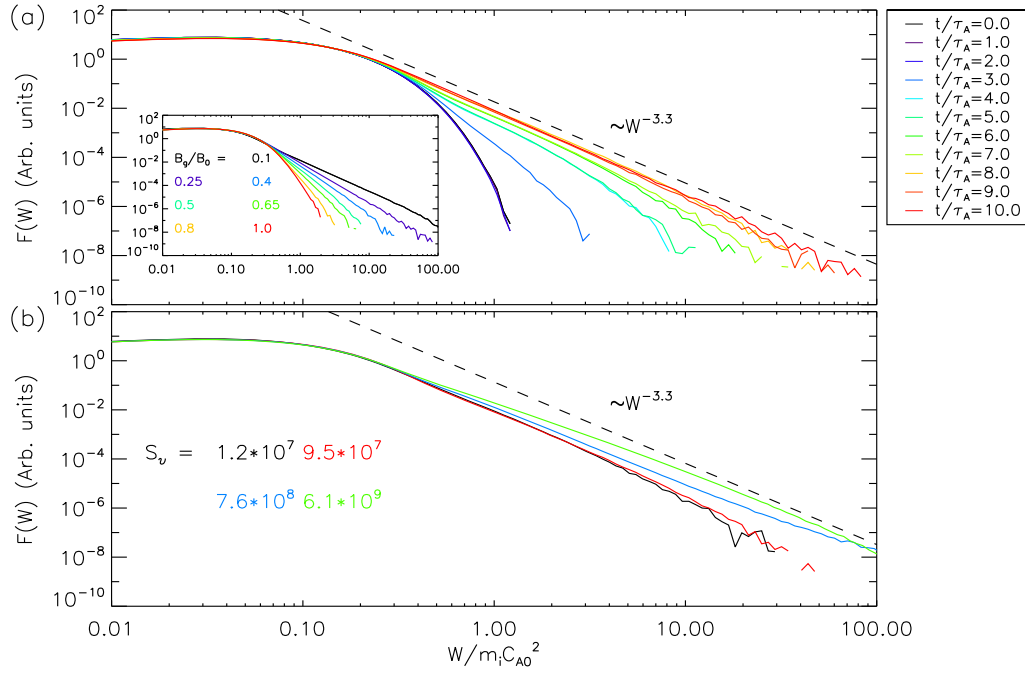
FIG. 2. In (a): a log-log plot of $F(W)$ versus energy at multiple times for the $B_g/B_0 = 0.25$ simulation. Inset in (a): the late time $F(W)$ for several guide fields. In (b): the late time $F(W)$ for $B_g/B_0 = 0.25$ with various values of S_ν (effective system size). The dashed line in both (a) and (b) is a power-law with $\delta' = 3.3$.

The inset in Fig. 2 shows the late-time $F(W)$ for several values of the guide field corresponding to times during the simulations when approximately the same amount of magnetic flux has reconnected. As the guide field decreases, δ' decreases so the spectrum becomes harder and more high-energy electrons are produced. In Fig. 2(b) we plot the late time spectrum of $F(W)$ for several values of S_ν. Larger values of S_ν correspond to larger systems. Thus, Fig. 2(b) demonstrates that the slope of the power-law of nonthermal electrons is relatively insensitive to the size of the system. However, the total energy contained in the nonthermal electrons increases with reconnected flux, and thus a larger system produces a more extended power-law.

The dependence of δ' on the guide field is plotted in the curve marked by the stars in Fig. 3(a). A strong guide field produces a soft nonthermal particle spectrum. The solid red curve is from the theoretical model discussed in the next section. Plotted in Fig. 3(b) is the time dependence of the energy of a typical electron that populates the power-law
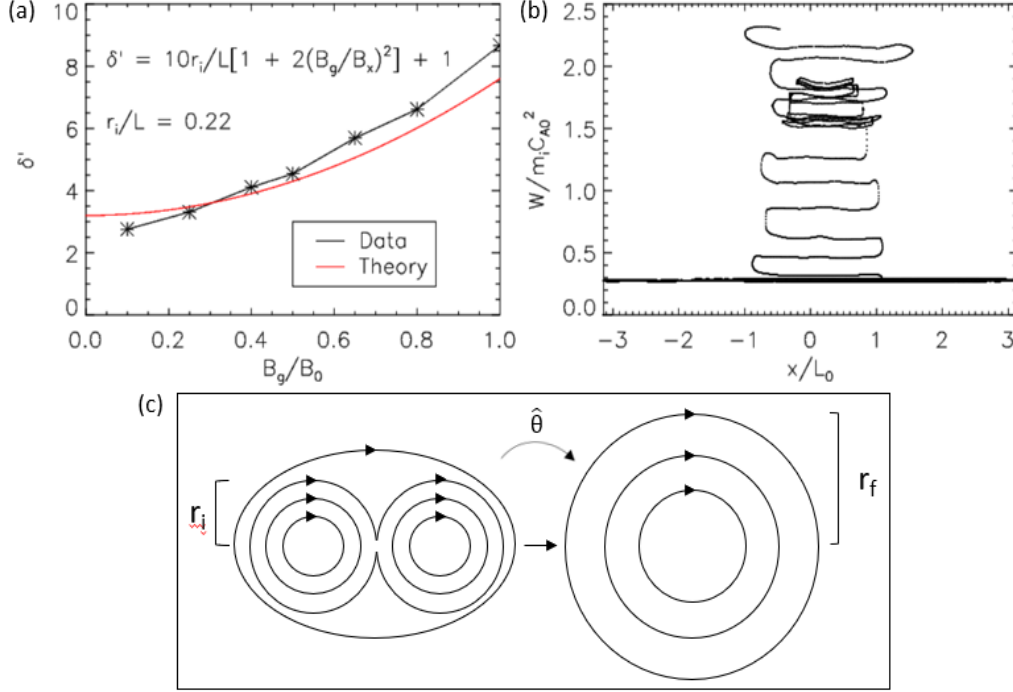
FIG. 3. In (a): δ' (black) versus guide field and the fit from the theoretical model (red). In (b): the energy versus x position of an electron that becomes a part of the nonthermal distribution. In (c): a schematic depicting the flux rope merging mechanism that leads to electron power-law distributions.

tail versus the x-position from a simulation with $B_g/B_0 = 0.25$. Early in time the electron makes several passes through the system with little change in energy. Once reconnection produces flux ropes, the electron is captured by a flux rope and, as it contracts and merges with other flux ropes, the electron undergoes Fermi reflection, gaining energy with each bounce. Fig. 3(c) is a schematic of the island-merging process that leads to the power-law tail (discussed in the following section).

In exploring the power-law distribution of nonthermal electrons, we averaged over the entire computational domain to improve the statistics of the number of electrons with very high energy. However, an important question in understanding particle energy gain during reconnection concerns the relative numbers and energy content of nonthermal electrons (those in the power-law tail) versus those that display a thermal or nearly thermal distribution. The observations suggest that the nonthermals often contain more energy than the hot thermals in large flares[4, 30, 31]. To explore these questions we analyzed data from

more limited spatial domains that include both hot thermal and nonthermal electrons but exclude electrons that have not yet gained energy from reconnection. We focus, therefore, on the interior of magnetic islands where the electron temperature has increased and where there are significant numbers of nonthermal electrons. The goals are to establish whether a characteristic effective temperature is associated with the hot thermal electrons and what fraction of the electrons can be categorized as hot thermal versus nonthermal.

Specifically, we explore the region between the two white ellipses within the middle flux rope in Fig. 1(c). In Fig. 4(a) we show $F(W)$ (black line) from the region between the two ellipses. The high-energy electrons form a power-law distribution even in this localized region within a single flux rope. In Fig. 4(b) we display the same data, but on a linear-linear scale focused on the lower energies to reveal the hot thermal population. These two plots reveal that localized regions within magnetic islands contain a mixture of electrons with a range of energies so that the characteristics of the hot thermal and nonthermals can be explored.

To model the distributions in Fig. 4 we use the sum of a Maxwellian and a kappa distribution. The kappa distribution fits the power-law tail of nonthermal electrons and the Maxwellian supplements the Maxwellian component of the kappa distribution at low energy, producing a good fit to the hot thermal electrons. The fitting procedure is discussed in detail in the Supplementary section [32]. The outputs of the fit to the electron distribution is the spectral index of the nonthermal electrons, and the number density and total energy content of the nonthermal and thermal electrons.

The results of fitting for all of the guide fields appear in Fig. 4, (c) and (d). Shown in (c) is the percentage of the total density (red) and energy (black) of the nonthermal electrons as defined in [32] as a function of the guide field. Each distribution that formed the basis of this data came from a region within an island similar to the one shown in Fig. 1(c). For a small guide field the energy content of the nonthermal electrons is $\sim 80\%$ of the total particle electron energy and $\sim 20\%$ of the total electron particle density. As the guide field increases, the number of nonthermal electrons and their energy content becomes small. In (d) is the total energy per particle of the particle electrons (black) and the corresponding energy per particle, or $(3/2)T_{th}$, of the hot thermal electrons (red), with the initial energy shown as a dotted line. This is further evidence that the nonthermal electrons dominate the total electron energy at low guide fields where the Fermi drive is strong. On the other
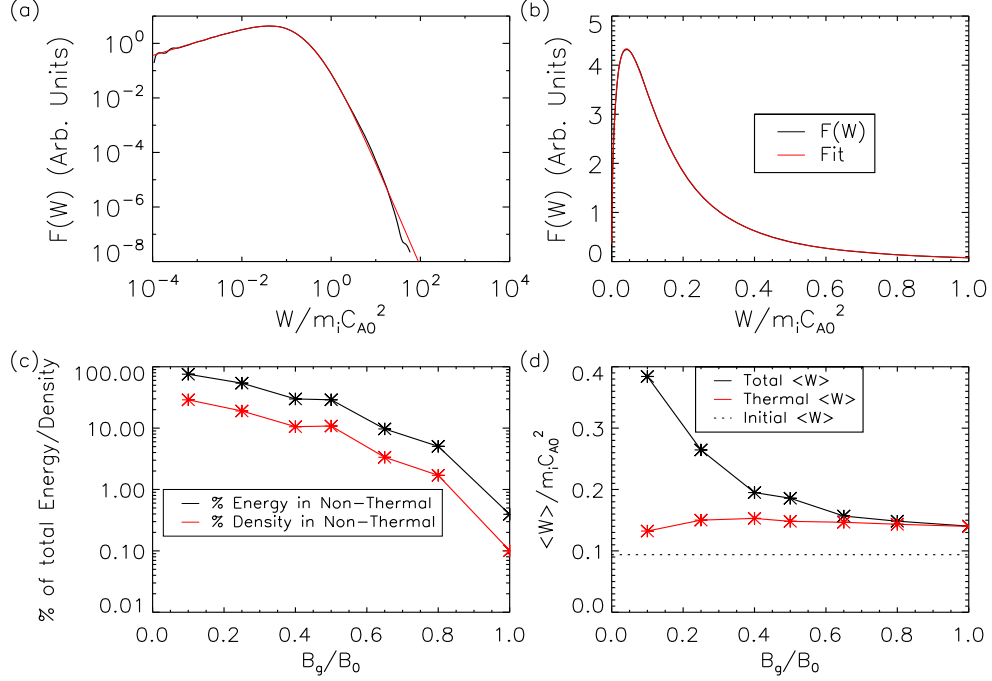
FIG. 4. In (a): $F(W)$ (black) along with the fit (red) described in the Supplementary section [32] versus energy on a log-log scale. In (b): the same data on a linear-linear scale, zoomed in to low energies to reveal the hot thermal electrons. In (c): the percentage of energy (black) and density (red) of nonthermal electrons versus guide field. In (d): the average energy per particle of particle electrons (black) and thermal electrons (red) versus guide field. The dotted line is the energy from the initial Maxwellian distribution of particle electrons.

hand, the energy of the hot thermal electrons is relatively insensitive to the guide field and is likely controlled by slow shocks (see [32]) rather than by Fermi reflection.

An analytic model for nonthermal electron acceleration We present a model for electron acceleration in a current layer with merging magnetic flux ropes that captures the essential results of the *kglobal* simulations, including an expression for the power-law index of the nonthermal electrons and its dependence on the ambient guide field. The model includes the convective loss of electrons injected into large, inactive flux ropes.

The model is based on electron energy gain during the merging of flux ropes. The dominant heating, parallel to the local magnetic field [10, 22], results from the shortening of field lines during flux rope mergers [16] as shown in Fig. 3(c): merging field lines contract from the figure-eight configuration on the left to the circle on the right. Parallel heating

9

results from the invariance of the parallel action $\oint v_\parallel dl$. Thus, the change in the energy during the merger of two flux ropes can be calculated by evaluating the geometry of the magnetic field before and after the merger. The calculation presented in the Supplementary section [32], results in the rate of energy gain

$$\dot{W} = \frac{d}{dt}W = W\frac{g}{\tau_r}, \tag{1}$$

with $\tau_r \sim r_i/Rc_{Ax}$ the merger time of a flux rope of initial radius r_i, where $R \sim 0.1$ is the normalized rate of merger of the flux ropes in the current layer, and c_{Ax} is the Alfvén speed based on the reconnecting magnetic field B_x. The factor $g = (1+2B_g^2/B_x^2)^{-1}$ arises from the dependence of the radius of curvature of the reconnecting magnetic field on the guide field [10, 11, 33]. With the energy gain in Eq. (7), an equation can be derived for the number density $F(x, W, t)$ of electrons per unit energy undergoing reconnection-driven acceleration in a one-dimensional current layer and experiencing convective loss,

$$\frac{\partial}{\partial t}F + \frac{\partial}{\partial x}v_x(x)F + \frac{\partial}{\partial W}\dot{W}F - D\frac{\partial^2}{\partial x^2}F = \frac{1}{\tau_{up}}F_{up} \tag{2}$$

where $v_x(x)$ describes the convective loss of electrons as they are ejected at the Alfvén speed out of the current layer and we include a simple constant diffusion of electrons within the current layer. The electrons are injected into the layer with an initial distribution F_{up} which is taken as a low-temperature Maxwellian. Although the simulations carried out here are periodic and particles are therefore not lost, the large flux ropes that emerge at late time and no longer participate in the reconnection process act as sinks for energetic electrons [18, 34]. For a low upstream temperature and strong diffusion D, the steady state solution to Eq. (2) is given by

$$F_0 \propto \frac{1}{W}W^{-c_{Ax}\tau_r/gL} \sim W^{-(1+r_i/gRL)}. \tag{3}$$

The energetic electron spectrum is a power-law with a spectral index that depends on the rate of reconnection R, the ratio of the characteristic radius r_i to the half-width L of the current layer and the relative strength of the guide field. A strong guide field for which $g \sim (2B_g^2/B_x^2)^{-1}$ produces a very soft electron spectrum. This scaling relation is compared with data from our simulations in Fig. 3(a). The best fit of the model with the data has $r_i/L = 0.22$, which is consistent with the typical scale of islands in the simulations.

Comparison with Observations The standard model for a solar flare comes from [35]. It includes an erupting flux rope that produces a large reconnecting current sheet with a cusp-shaped flare arcade below. As reconnection proceeds, more small flux ropes are produced

in the current sheet and flow either up toward the erupting flux rope, or down toward the arcade. The solar flare of September 10, 2017, was observed by several instruments [36–39]. The gyrosynchrotron spectrum revealed relativistic electrons throughout the reconnecting current sheet, with an increase in intensity where the current sheet meets the arcade. The observed power-law indices, $\delta`$, for this region fell in the range 3.5-6.5, depending on the position. The RHESSI observations for this event revealed both a footpoint and an extended coronal source [36]. The coronal source had a photon spectral index near 4.4, which for thin target emission corresponds to a particle spectral index $\delta' = 3.9$. Late in the flare the temperature of the hot thermal electrons in the coronal current sheet was analyzed with the EIS Fe XXIV/Fe XXIII ratio [37]. The hot thermal electron temperature had a broad peak near 2.5keV.

Our simulations reveal that the spectral index of nonthermal electrons and the number of the nonthermals depends strongly on the ambient guide field. Comparisons of MHD simulations of the September 10, 2017, flare with gyrosynchrotron emission of energetic electrons revealed that the guide field was 30% of the reconnecting magnetic field [38]. Based on the data from Fig. 2, our simulations predict a power-law index near 3.5, within the range measured from gyrosynchrotron emission and very close to the RHESSI measurement.

We can also compare the temperature jump of the hot thermal electrons in our simulation with the measured 2.5keV from the EIS data. The simulation data in Fig. 4(d) suggests that the hot thermal electrons should have a temperature jump near $0.04 m_i C_{A0}^2$. The Alfvén speed was estimated as 6,000 to 10,000 km/s [38], which yields a temperature of 15-42keV, well above the observations. On the other hand, such high flow speeds were not measured. At the time of the EIS observations the measured outflow speed in the current sheet was $\sim$ 800km/s [40], which is likely a lower bound because of projection effects. Further, *in situ* measurements at 1AU indicate that the outflow speed is around 2/3 of the upstream Alfvén speed [41]. Using 1200km/s for C_{A0}, we calculate a hot electron temperature of 0.6keV, which is smaller than the EIS measurement. Thus, more precise measurements of the outflow speed are needed.

Observations of large numbers of flares have revealed that the energy in nonthermal electrons exceeds that of the thermal electrons in $\sim$ 80% of events, suggesting that solar flares are extremely efficient at accelerating nonthermal electrons [30]. The efficiency of nonthermal electron acceleration was greatest in large flares [31] although recent evidence

11

from NuSTAR suggests that such results might extend to smaller flares [42]. Such results are consistent with Fig. 4(c) if $B_g/B_0 < 0.4$. The simulations (Fig. 2(b)) further suggest that even small flares might be efficient sources of nonthermal electrons.

An important question is why conventional PIC modeling has been unable to produce the extended power-law spectra that develop in kglobal. Some groups have been able to produce power-laws, such as [44] and [18], however, they only extend about a decade in energy and they do not establish the dependence on the guide field. We suggest that the short power-laws seen in PIC is because of inadequate separation between kinetic scales and the macro-system scale. As electrons gain energy from Fermi reflection in the PIC model, their Larmor radii become comparable to the reconnecting flux ropes in the system and they become unmagnetized [18]. This suppresses energy gain associated with Fermi reflection [16]. In PIC simulations the problem is extreme because the macroscale in flares is of the order of $10^4 km$ while the simulation domains are of the order of 100's of meters. The artificially large electron masses in PIC models further exacerbate the problem. In a real flaring system the Larmor radii of electrons with energies of 10's of MeV remain small so electron demagnetization in reconnecting flux ropes is not likely to be important. In kglobal the reconnecting flux ropes are at the macroscale and the electron dynamics is guiding center and therefore fully magnetized.

SUPPLEMENTAL

Electron energy gain As has been reported in previous PIC simulations we have monitored the three mechanisms by which the particle electrons gain energy as a function of time: Fermi reflection, the parallel electric field, and betatron acceleration [22]. The data for guide fields $B_g/B_0 = 1.0$ and 0.1 are shown in Fig. 5(a) and (b), respectively. As in earlier simulations, electron energy gain is bursty, which reflects the periodic merger of finite size flux ropes. In the case of a weak guide field Fermi reflection dominates energy gain during the entire simulation while acceleration by the betatron mechanism (corresponding to the conservation of the magnetic moment $V_\perp^2/B$) and the parallel electric field are negligible. For a strong guide field betatron acceleration is again negligible while acceleration by the parallel electric field becomes comparable to the Fermi mechanism at late time. Notably, there is an increase in heating due to $E_\parallel$ toward the end of the simulation for $B_g/B_0 = 1$. This is likely due to the development of the large scale $E_\parallel$ that forms after the electrons injected into the reconnection exhaust gain significant energy. At this point the resulting potential drop can heat electrons entering the exhaust as documented in PIC simulations [23, 25]. This effect is subdominant in comparison to Fermi reflection for the case of a small guide field. Note, however, that the overall electron heating rate for the strong guide field case is more than an order of magnitude lower than in the case of a weak guide field.

In Fig. 5(c) the parallel electric field is shown at late time. The large-scale electric field points away from the current sheet in the outflow exhausts as expected since the parallel electric field serves to prevent hot electrons from escaping upstream [23–25]. To see that the electric field points away from the current sheet, note that B_x is positive above the current sheet and negative below so that B_y is positive on the left side of the left-most flux rope. Thus, $E_\parallel \sim E_y$ is positive above the current sheet and negative below. The unusual vertically oriented structures in $E_\parallel$ correspond to the locations of slow shocks that propagate to the left and right in the simulation. The *kglobal* model correctly describes the potential drop across the slow shock that maintains charge neutrality. The slow shocks produced during reconnection are not effective in driving the nonthermal electrons [43]. However, the electron distribution across the slow shock reveals electron reflection and acceleration that likely causes heating of the thermal electrons and leads to the thermal energy gain seen in Fig. 4(d). This heating can also be observed in the upstream region in Fig. 5(d), which
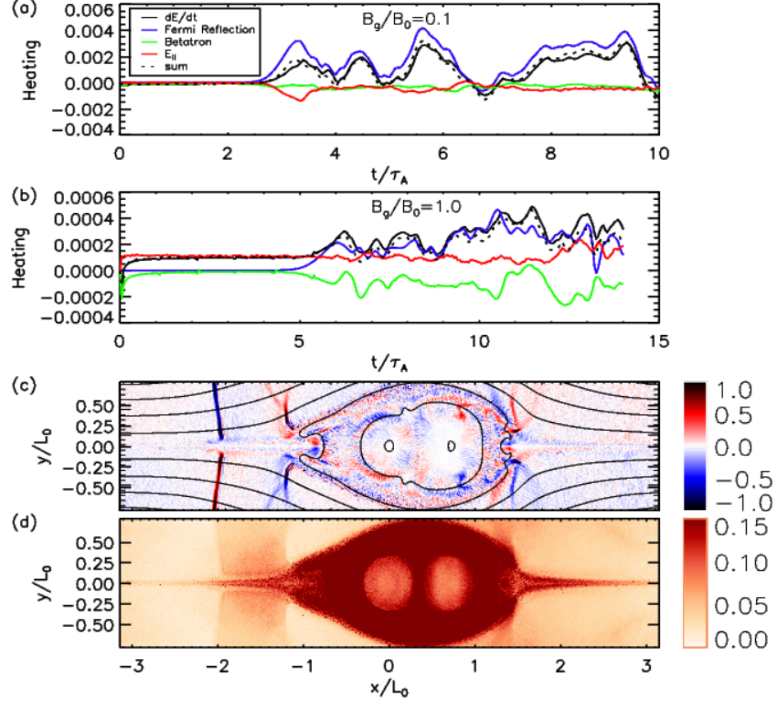
FIG. 5. In panel (a): the heating of the particle electrons due to Fermi reflection (blue), the large scale parallel electric field (red), betatron acceleration (green), the sum of the previous three (dashed black), and the measured heating (black) versus time for $B_g/B_0=1.0$. In panel (b): the same but for $B_g/B_0 = 0.1$. In panel (c) and (d): the parallel electric field with field lines overplotted and $< W_{||} >$ respectively at late time for $B_g/B_0 = 0.025$ and initial electron temperature 0.02.

shows the average parallel energy per particle electron and has been overexposed to show the upstream heating associated with the slow shocks. This heating process will be explored in a future paper.

Fitting procedure of the particle electron distributions To model the electron distribution functions in Fig. 4 we use the sum of a Maxwellian and a kappa distribution. The functional forms of the two distributions are shown in Eq. 4. Since the kappa function only has two free parameters, we include the Maxwellian component to capture the power

law index, the thermal temperature, and the relative number of nonthermal electrons.

$$F_{fit}(W) = F_\kappa(W) + F_M(W) =$$

$$\left[\frac{N_\kappa}{(\pi\kappa\theta^2)^{3/2}} \frac{\Gamma(\kappa+1)}{\Gamma(\kappa-1/2)} \left(1 + \frac{W}{\kappa\theta^2}\right)^{-(\kappa+1)} + \right. \tag{4}$$

$$\left. N_M \left(\frac{m_e}{2\pi T_M}\right)^{3/2} e^{-W/T_M} \right] 4\pi\sqrt{\frac{2W}{m_e^3}}$$

where $F_{fit}(W)$ is the fit to the total electron differential density, N_κ is the density of the kappa function, θ is the most probable speed in the kappa function, Γ is the Gamma function, N_M is the density of the Maxwellian function, m_e is the electron mass, T_M is the temperature (in energy units) of the Maxwellian, and W is the energy. Note that $\int F_{fit}(W)dW = N_\kappa + N_M$. Since the kappa function is a Maxwellian in the limit of low energy, we can further break up F_{fit} into a Maxwellian component, $F_M(W)$, a Maxwellian component from the kappa function, $F_{\kappa M}(W)$, and a nonthermal component from the kappa function that includes the power-law tail, $F_{\kappa NT}(W)$. To do this we follow the method laid out in [27]. We define a second Maxwellian temperature, $T_{\kappa M} \equiv (1/2)m_e\theta^2$, and set $F_{\kappa M}(T_M) = F_\kappa(T_M)$. This gives us an expression for the relative density and energy of the nonthermal electrons:

$$N_{NT} = N_\kappa - N_{\kappa M} =$$

$$N_\kappa \left(1 - 2.718 \frac{\Gamma(\kappa+1)}{\Gamma(\kappa-1/2)} \kappa^{-3/2} \left(1 + \frac{1}{\kappa}\right)^{-(\kappa+1)}\right) \tag{5}$$

$$<W_{NT}> = <W_\kappa> - <W_{\kappa M}> = \frac{3}{2}T_\kappa - \frac{3}{2}T_{\kappa M} \tag{6}$$

where $T_\kappa = (1/2)m_e\theta^2[\kappa/(\kappa-3/2)]$. F_{fit} is overlaid in red on top of the particle data (in black) in the log-log plot in Fig. 4(a). In (b) F_{fit} is again overlaid in red over the particle data, but on a linear-linear scale zoomed in to low energies to more clearly see the thermal population. The dual Maxwellian-kappa function fits both the low and high energy particle data very well and can therefore be used to explore the relative numbers of hot thermal versus nonthermal electrons and the characteristic temperature of the hot thermals.

Analytic model of electron acceleration in a current sheet We present a model for electron acceleration in a current layer with merging magnetic flux ropes that captures the essential results of the *kglobal* simulations, including an expression for the power-law index of the nonthermal electrons and its dependence on the ambient guide field. The model includes

both diffusion along the current layer as well as the convective loss of electrons injected into large, inactive flux ropes.

We first calculate electron energy gain during the merging of two flux ropes of radius r_i, azimuthal magnetic $B_{\theta i}$ and guide field B_g as shown in Fig. 3(c). Consistent with extensive PIC simulation results that the dominant electron heating is parallel to the local magnetic field [10, 22], we neglect plasma compression and associated betatron acceleration. Parallel heating results from the invariance of the parallel action $\oint v_{\parallel} dl$ as merging field lines contract from the figure-eight on the left of Fig. 3(c) to the circle on the right. Thus, the change in the energy during the merger of two flux ropes can be calculated by evaluating the geometry of the magnetic field before and after the merger. For an incompressible merger, the radius of the final flux rope is $r_f = \sqrt{2} r_i$ and the flux is preserved $r_f B_{\theta f} = r_i B_{\theta i}$ [16]. The effective field line length of the initial state is twice the length of a single flux rope, $s_i = 2\pi r_i B_i / B_{\theta i}$, where $B_i^2 = B_g^2 + B_{\theta i}^2$, since a reconnecting field line wraps around both flux ropes as can be seen by the recently reconnected field line in Fig. 3(c),. The final field line length is $s_f = 2\pi r_f B_f / B_{\theta f}$. Thus, invoking the invariance of the parallel action, the final electron parallel energy W_f is given by $W_i s_i^2 / s_f^2$. The energy change can be re-written as a rate equation for electron energy gain

$$\dot{W} = \frac{d}{dt} W = W \frac{g}{\tau_r}, \tag{7}$$

with $\tau_r \sim r_i / R c_{Ax}$, where $R \sim 0.1$ is the normalized rate of merger of the flux ropes in the current layer, c_{Ax} the Alfvén speed based on the reconnecting magnetic field B_x of the current layer, and the factor $g = (1 + 2 B_g^2 / B_x^2)^{-1}$. The factor g describes the increase of the effective radius of curvature of the magnetic field in the presence of a guide field, which reduces the strength of Fermi reflection and associated energy gain during reconnection [10, 11, 33].

With the energy gain in Eqn. (7), we can write down an equation for the number density $F(x, W, t)$ of electrons per unit energy undergoing reconnection driven acceleration in a one-dimensional current layer and experiencing convective loss,

$$\frac{\partial}{\partial t} F + \frac{\partial}{\partial x} v_x(x) F + \frac{\partial}{\partial W} \dot{W} F - D \frac{\partial^2}{\partial x^2} F = \frac{1}{\tau_{up}} F_{up} \tag{8}$$

where $v_x(x)$ describes the convective loss of electrons as they are ejected at the Alfvén speed out of the current layer and we include a simple constant diffusion of electrons within the

current layer. The electrons are injected into the layer with an initial distribution F_{up} which is taken as a low-temperature Maxwellian. Although the simulations carried out here are periodic and particles are therefore not lost, the large flux ropes that emerge at late time and no longer participate in the reconnection process act as sinks for energetic electrons [18, 34].

Further, as magnetic flux continues to be added to these flux ropes, electrons trapped in the islands become disconnected from the current layers. As in the classical problem of diffusive shock acceleration, the boundary condition on f at the injection point into the flux rope is zero slope.

The steady state solution of Eq. (8) can be written as a sum of harmonics of $F \sim \sum_n F_n \cos(n\pi x/L)$, where we take the current layer to be centered at $x = 0$ and the injection in the large flux ropes to take place at $x = \pm L$ at the Alfvén speed c_{Ax}. However, the problem is simplified if the diffusion D is large so that the harmonics F_n with $n \neq 0$ are small. In this limit Eqn. (8) can simply be integrated over x to obtain an expression for F_0,

$$L\frac{\partial}{\partial W}\frac{Wg}{\tau_w}F_0 + c_{Ax}F_0 = \frac{L}{\tau_{up}}F_{up}. \tag{9}$$

This equation is readily inverted for F_0,

$$F_0 = \frac{1}{\tau_{up}}\frac{\tau_r}{gW}W^{-c_{Ax}\tau_r/gL}\int_0^W dW W^{c_{Ax}\tau_r/gL}F_{up}(W). \tag{10}$$

For low upstream temperature the energy integral can be extended to infinity and F_0 has the scaling

$$F_0 \propto \frac{1}{W}W^{-c_{Ax}\tau_r/gL} \sim W^{-(1+r_i/gRL)}. \tag{11}$$

The energetic spectrum takes the form of a power-law with a spectral index that depends on the rate of reconnection R, the relative size of the merging flux ropes that drive electron energy gain compared with the half-width of the current sheet L and the strength of the guide field.

---

[1] Lin, R. P., & Hudson, H.S. (1971). 10-100 keV electron acceleration and emission from solar flares, *Solar Physics* 17, 412-435

[2] Emslie, A. G., Kucharek, H., Dennis, B. R., Gopalswamy, N., Holman, G. D., Share, G. H. et

al. (2004). Energy partition in two solar flare/CME events, *Journal of Geophysical Research* 109, A10104

[3] Emslie, A. G., Dennis, B. R., Holman, G. D., & Hudson, H. S. (2005). Refinements to flare energy estimates: A followup to "Energy partition in two solar flare/CME events" by A. G. Emslie et al., *Journal of Geophysical Research* 110, A11103

[4] Emslie, A. G., Dennis, B. R., Shih, A. Y., Chamberline, P. C., Mewaldt, R. A., & Moore, C. S. (2012). Global Energetics of Thirty-Eight Large Solar Eruptive Events, *The Astrophysical Journal* 759, 71

[5] Heristchi, D., & Amari, T. (1992). Solar flare high-energy electron spectra, *Solar Physics* 142, 209-211

[6] Krucker, S., Hudson, H. S., Glesener, L., White, S. M., Masuda, S., Wuelser, J.-P., & Lin, R. P. (2010). Measurements of the coronal acceleration region of a solar flare, *The Astrophysical Journal* 714, 1108-1119

[7] Oka, M., Phan, T. D., Krucker, S., Fujimoto, M., & Shinohara, I. (2010). Electron Acceleration by Multi-Island Coalescence *The Astrophysical Journal* 714, 1

[8] Øieroset, M., Lin, R. P., Phan, T. D., Larson, D. E., & Bale, S. D. (2002). Evidence for Electron Acceleration up to 300 keV in the Magnetic Reconnection Diffusion Region of Earth's Magnetotail *Physical Review Letters* 89, 195001

[9] Drake, J. F., Shay, M. A., Thongthai, W. & Swisdak, M. (2006). Production of Energetic Electrons during Magnetic Reconnection, *Physical Review Letters* 94, 095001

[10] Dahlin, J. T., Drake, J. F., & Swisdak, M. (2017). The role of three-dimensional transport in driving enhanced electron acceleration during magnetic reconnection, *Physics of Plasmas* 24, 092110

[11] Drake, J. F., Swisdak, M., Che, H., & Shay, M. (2006). Electron acceleration from contracting magnetic islands during reconnection, *Nature* 443, 553-556

[12] Drake, J. F., Opher, M., Swisdak, M., & Chamoun, J. N. (2010). A Magnetic Reconnection Mechanism for the Generation of Anomalous Cosmic Rays, *The Astrophysical Journal* 709, 2

[13] Krucker, S. & Battaglia, M. (2014). Particle densities within the acceleration region of a solar flare, *The Astrophysical Journal* 780, 107

[14] Parker, E. N. (1957). Sweet's Mechanism for Merging Magnetic Fields in Conducting Fluids *Journal of Geophysical Research* 62, 4

[15] Lin, Y., & Lee, L. C. (1993). Structure of the dayside reconnection layer in resistive MHD and hybrid models, *Journal of Geophysical Research Space Physics* 98, A3

[16] Drake, J. F., Swisdak, M., & Fermo, R. (2013). The power-law spectra of energetic particles during multi-island magnetic reconnection, *The Astrophysical Journal Letters* 763, L5

[17] Guo, F., Li, H., Daughton, W., & Liu, Y. (2014). Formation of Hard power-laws in the Energetic Particle Spectra Resulting from Relativistic Magnetic Reconnection, *Physical Review Letters* 113, 155005

[18] Li, X., Guo, F., Li, H., Stanier, A., & Kilian, P. (2019). Formation of Power-law Electron Energy Spectra in Three-dimensional Low-β Magnetic Reconnection, *The Astrophysical Journal* 884, 118

[19] Fermo, R. L, Drake, J. F., & Swisdak, M. (2010). A Statistical Model of Magnetic Islands in a Current Layer, *Physics of Plasmas* 17, 010702

[20] Drake, J. F., Arnold, H., Swisdak, M., & Dahlin, J. T. (2019). A computational model for exploring particle acceleration during reconnection in macroscale systems, *Physics of Plasmas* 26, 012901

[21] Arnold, H., Drake, J., Swisdak, M., & Dahlin, J. (2019). Large-scale parallel electric fields and return currents in a global simulation model, *Physics of Plasmas* 26, 102903

[22] Dahlin, J. T., Drake, J. F., & Swisdak, M. (2014). The mechanisms of electron heating and acceleration during magnetic reconnection, *Physics of Plasmas* 21, 092304

[23] Egedal, J., Daughton, W., & Le, A. (2012). Large-scale electron acceleration by parallel electric fields during magnetic reconnection, *Nature Physics* 8, 32-324

[24] Egedal, J., Daughton, W., Le, A., & Borg, A. L. (2015). Double layer electric fields aiding the production of energetic flat-top distributions and superthermal electrons within magnetic reconnection exhausts, *Physics of Plasmas* 22, 101208

[25] Haggerty, C. C., Shay, M. A., Drake, J. F., Phan, T. D., & McHugh, C. T. (2015). The competition of electron and ion heating during magnetic reconnection, *Geophyscial Research Letters* 42, 9657-9665

[26] Lin, R. P., Krucker, S., Hurford, G. J., Smith, D. M., Hudson, H. S., Holman, G. D., Schwartz, R. A., Dennis B. R., Share, G. H., Murphy, R. J., Emslie, A. G., Johns-Krull, C., & Vilmer, N. (2003). RHESSI Observations of Particle Acceleration and Energy Release in an Intense Solar Gamma-Ray Line Flare, *The Astrophysical Journal Letters* 595, 2

[27] Oka, M., Ishikawa, S., Saint-Hilaire, P., Krucker, S., & Lin, R. P. (2013). Kappa distribution model for hard x-ray coronal sources of solar flares *The Astrophysical Journal* 764, 6

[28] Kaw, P. K., Valeo, E. J., & Rutherford, P. H. (1979). Tearing Modes in a Plasma with Magnetic Braiding, *Physical Review Letters* 43, 1398

[29] Oka, M., Birn, J., Battaglia, M., Chaston, C., Hatch, S., Livadiotis, G., Imada, S., Miyoshi, Y., Kuhar, M., Effenberger, F., Eriksson, E., Khotyaintsev, Y., & Retinò, A. (2018). Electron Power-Law Spectra in Solar and Space Plasmas *Space Science Reviews* 214, 82

[30] Aschwanden, M., Holman, G., O'Flannagain, A., Caspi, A., McTiernan, J., & Kontar, E. (2016). Global Energetics of Solar Flares. III. Nonthermal Energies, *The Astrophysical Journal* 832, 27

[31] Warmuth, A. & Mann, G. (2016). Constraints on energy release in solar flares from RHESSI and GOES X-ray observations, *Astronomy and Astrophysics* 588, A115

[32] See Supplemental Material at [URL will be inserted by publisher] for a discussion on electron heating, a description of how we fit the electron distribution function, and a description of our analytic model for calculating the power law index of the electrons.

[33] Dahlin, J. T., Drake, J. F., & Swisdak, M. (2016). Parallel electric fields are inefficient drivers of energetic electrons in magnetic reconnection, *Physics of Plasmas* 23, 120704

[34] Dahlin, J. T., Drake, J. F., & Swisdak, M. (2015). Electron acceleration in three-dimensional magnetic reconnection with a guide field, *Physics of Plasmas* 22, 100704

[35] Lin, J., & Forbes, T. G. (2000). Effects of reconnection on the coronal mass ejection process, *Journal of Geophysical Research* 105, 2375-2392

[36] Gary, D. E., Chen, B., Dennis, B. R., Fleishman, G. D., Hurford, G. J., Krucker, S., McTiernan, J. M., Nita, G. N., Shih, A. Y., & White, S. M. (2020). Microwave and Hard X-Ray Observations of the 2017 September 10 Solar Limb Flare, *The Astrophysical Journal Letters* 863, 1

[37] Warren, H. P., Brooks, D. H., Ugarte-Urra, I., Reep, J. W., Crump, N. A., & Doschek, G. A. (2018). Spectroscopic Observations of Current Sheet Formation and Evolution *The Astrophysical Journal* 854, 2

[38] Chen, B., Shen, C., Gary, D., Reeves, K., Fleishman, G., Yu, S., Guo, F., Krucker, S., Lin, J., Nita, G., & Kong, X. (2020). Measurement of Magnetic Field and Relativistic Electrons along a Solar Flare Current Sheet, *Nature Astronomy Letters*

[39] Fleishman, G. D., Gary, D. E., Chen, B., Kuroda, N., Yu, S., & Nita, G. M. (2020). Decay of the coronal magnetic field can release sufficient energy to power a solar flare, *Science* 367, 6475

[40] Cheng, X., Li, Y., Wan, L. F., Ding, M. D., Chen, P. F., Zhang, J., & Liu, J. J. (2018). Observations of Turbulent Magnetic Reconnection within a Solar Current Sheet, *The Astrophysical Journal* 866, 1

[41] Haggerty, C., Shay, M., Chasapis, A., Phan, T., Drake, J. F., Malakit, K., Cassak, P., & Kieokaew, R. (2018). The reduction of magnetic reconnection outflow jets to sub-Alfvénic speeds, *Physics of Plasmas* 25, 102120

[42] Glesener, L., Krucker, S., Duncan, J., Hannah, I., Grefenstette, B., Chen, B., Smith, D., White, S., & Hudson, H. (2020). Accelerated Electrons Observed Down to ¡7 keV in a NuSTAR Solar Microflare, *The Astrophysical Journal Letters* 891, 2

[43] Zhang, Q., Drake, J. F., & Swisdak, M. (2019). Instabilities and Turbulence in Low-β Guide Field Reconnection Exhausts with Kinetic Riemann Simulations *Physics of Plasmas* 26, 102115

[44] Baumann, G., Haugbølle, T. and Nordlun, Å (2013). Kinetic Modeling of Particle Acceleration in a Solar Null-Point Reconnection Region *The Astrophysical Journal* 771, 2